NJC

ROYAL SOCIETY OF CHEMISTRY

PAPER

View Article Online
View Journal | View Issue

Cite this: *New J. Chem.*, 2025, **49**, 4813

Oxygen activation on a carbon catalyst support co-doped with Si and transition metals: an electrochemical study†

Timon Schönauer,‡[a] Thierry K. Slot,‡[b] Karina Ioffe,[b] Yair Shahaf,[b] Rhett Kempe*[a] and David Eisenberg*[b]

Received 11th December 2024,
Accepted 11th February 2025

DOI: 10.1039/d4nj05300a

rsc.li/njc

Multi-doped carbons are promising thermocatalysts, electrocatalysts, and catalyst supports. Recently, Si-co-doped carbons have emerged as catalyst supports for a range of reductive coupling reactions. However, little is known about their catalytic activity in the oxygen cycle. We now report a detailed electrochemical and material investigation into a range of Si-doped carbons, aimed at correlating their activity towards the reduction of O_2 and H_2O_2 with their composition and structure. We examine a broad range of pyrolysis temperatures (600–1000 °C), combined with several oxygen-active metals (Ag, Mn, Co), co-doped into the Si-, N-doped support either alone or in combinations at different ratios. Using a combination of X-ray diffraction, XPS and Raman spectroscopies, electron microscopy and elemental analysis, we identify the factors contributing to O_2 activation (as expressed in electrochemical O_2 reduction in alkaline) and reactivity towards H_2O_2 production and further reduction. As a result, the precise combination of metal dopants, ratios, and pyrolysis temperatures is identified as optimal for $2e^-/4e^-$ selectivity in O_2 reduction and total H_2O_2 yield. We hope that these findings will enable better rational design of Si-codoped catalysts supports for many thermocatalytic and electrocatalytic reactions.

Introduction

Carbon is an important material for both heterogeneous catalysis[1–3] and electrocatalysis.[4] Carbon offers mechanical support for active sites, high surface area, mass transfer of reactants and products in the porous network, electrical conductivity between the electrocatalytic sites and the external surface, and rich surface chemistry to bind and activate reactants.[5–8] In particular, the binding and reactivity of O_2 is of interest both to the electrocatalysis community centred on O_2 reduction (as in fuel cells,[7,9] metal–air batteries,[10,11] or H_2O_2 synthesis electrolyzers[12]), and for the heterogeneous catalysis community interested in heterogeneous oxidation reactions.[6,8]

On its own, carbon is neither a great thermal catalyst[13] nor electrocatalyst.[14] Once dopants are added, however, its electronic structure and surface chemistry change drastically.[15] The most popular nonmetal dopants are N, P, S B, and the halogens.[16,17] Lately, atomically dispersed N-coordinated metal ions (*e.g.* $M–N_4$, where M = Fe, Co, Cu, Ni) became useful for electrocatalysis[18–21] and heterogeneous catalysis[22,23] of many important reactions.

Recently, the Kempe group discovered a family of carbons co-doped with silicon and nitrogen (NSiCs) which serve as excellent supports for heterogeneous catalysts.[2,3,24] Silicon is an uncommon dopant in carbon-based catalysts,[25] since it reacts during pyrolysis to form inactive and insulating phases like SiC, SiO_2, or SiN.[26] Nevertheless, the presence of Si atoms could changes the local electronic structure in the carbon network,[27] promote sp^3 hybridization, influence the adsorption of reactants,[28] and possibly provide anchoring points for catalytic metal particles. Si-doping in the carbon lattice can induce structural deformations and change the local surface curvature, enhancing the splitting of N–H and O–H bonds.[29] Co-doping with Si and N facilitates activation of O_2 and desorption of H_2O during the oxygen reduction reaction (ORR) in acid.[25] In alkaline conditions, excellent ORR activity was reported on Si-, N-doped carbon nanotubes ($E_{\frac{1}{2}}$ = 0.86 V *vs.* RHE, 0.1 M KOH), as well as increased stability and methanol tolerance.[30] A high electron transfer number of 3.83 e^- per mole of O_2 was reported on Si-rich carbons (with or without N).[31] However, the combination of these dopants with other metals has not been

[a] *Lehrstuhl Anorganische Chemie II, Universität Bayreuth, 95440 Bayreuth, Germany. E-mail: kempe@uni-bayreuth.de*
[b] *Schulich Faculty of Chemistry, The Grand Technion Energy Program, and the Resnick Sustainability Center for Catalysis, Technion – Israel Institute of Technology, Haifa 3200003, Israel. E-mail: eisenberg@technion.ac.il*

† Electronic supplementary information (ESI) available: Material characterizations and electrochemical measurements. See DOI: https://doi.org/10.1039/d4nj05300a

‡ T. S. and T. K. S. contributed equally and can be interchanged in the order of authorship.

investigated, which is the case for supported catalysts. Thus, we need a better understanding of the role and interactions of Si and N dopants with carbon and with metal particles, in particular for the activation of oxygen and peroxide, key reactants and intermediates in oxidation reactions.[5,8,32]

We now report an electrochemical investigation into the oxygen activation ability of carbons co-doped with Si-, N-, and M = Mn, Co, Ag. By studying their activity towards multi-step ORR (eqn (1)–(3)), we can identify the synthetic, compositional and structural parameters most important for activation of O_2 and H_2O_2. We further investigate how the reactivity changes when the NSiC support is loaded with a broad range of oxygen-activating metallic particles, including combinations of Mn, Co, and Ag. We hope that the improved understanding of the different interactions will allow better design of both electrocatalysts, and catalyst supports for heterogeneous oxidation reactions.

$$O_2 + H_2O + 2e^- \rightleftharpoons HO_2^- + OH^- \quad E_{\frac{1}{2}} = -0.065\ \text{V } \textit{vs.}\ \text{SHE} \tag{1}$$

$$HO_2^- + H_2O + 2e^- \rightleftharpoons 3\ OH^- \quad E_{\frac{1}{2}} = 0.867\ \text{V } \textit{vs.}\ \text{SHE} \tag{2}$$

$$HO_2^- \rightleftharpoons \tfrac{1}{2}\ O_2 + OH^- \tag{3}$$

Experimental procedures

Synthesis of the NSiC-*T* materials

The NSiC materials were synthesized according to a known procedure.[24] 0.200 g StarPCS™ SMP-10, 0.988 mL (0.800 g, 15.08 mmol) acrylonitrile (AN) and 0.075 g (0.46 mmol) azobisisobutyronitrile (AIBN) were dissolved in 4 mL dimethylformamide (DMF) and heated up to 75 °C for 20 h under air. After solvent removal, the resulting yellowish solid was pyrolyzed under N_2 atmosphere. The heating program is illustrated in Scheme S1 (ESI†). Briefly, starting from room temperature (RT), the sample was heated to 200 °C (5 K min^{-1}), then to 400 °C (1 K min^{-1}), and finally to the desired pyrolysis temperature, *T,* (Table S1, 5 K min^{-1}, ESI†) and held there for 1 h, after this time, the sample cooled down to RT (5 K min^{-1}).

The sample was ball-milled for 40 min and 500 mg support material was washed under stirring in an aqueous solution of 1 M NaOH (6.7 mL) and MeOH (5 mL) at 90 °C for 20 h under air. The material was washed with double deionized water (DDI, >18.2 MΩ) until pH 7 was reached. The material was weighed before and after the procedure to determine the ceramic amount (see Table S1, ESI†). The NSiC-*T* materials were obtained in a yield of 55–69%.

Synthesis of the Co-, Mn- and Ag-loaded materials

To an aqueous solution (20 mL H_2O) of the metal salt (see Table S2 in the ESI† for details), 500 mg NSiC-*T* material was added, and the suspension was evaporated under stirring at 105 °C. After evaporation, the sample was pyrolyzed under nitrogen atmosphere at 700 °C followed by reduction at 550 °C (N_2/H_2, 90/10, v/v), following the heating program as described below (see also Scheme S2, ESI†). In short, starting from RT, the sample was heated to 300 °C (2 K min^{-1}) under nitrogen, then to 700 °C (10 K min^{-1}) and kept there for 30 min. The sample was cooled to 100 °C at (20 K min^{-1}) under nitrogen. Reduction was performed by heating the sample to 550 °C (5 K min^{-1}) under N_2/H_2 (90/10, v/v), and kept there for 3 h. Finally, the sample was cooled down to 40 °C (20 K min^{-1}) under nitrogen N_2/H_2.

Synthesis of the bimetal loaded materials

To an aqueous solution (20 mL H_2O) of the two metal salts (see Table S3, ESI†), 500 mg $NSiC_{1000}$ material was added and the suspension was evaporated under stirring at 105 °C. After evaporation, the sample was pyrolyzed under nitrogen atmosphere at 700 °C, followed by reduction at 550 °C (N_2/H_2, 90/10) with the same heating program as for the single metal materials (Scheme S2, ESI†).

HCl treatment of the catalysts

200 mg of the respective catalyst was suspended in 100 mL of hydrochloric acid (32%). The suspension was heated (80 °C) for 30 min and then stirred for 20 h at RT. The material was washed with DDI water until pH 7 was reached in the filtrate.

Electrochemical characterization

Electrochemical measurements for the oxygen reduction reaction (ORR) were recorded on a bipotentiostat (BioLogic 600) combined with a Pine rotating electrode setup, using a three-electrode glass cell, filled with KOH (0.1 M, 100 mL), and stabilized at 25.0 ± 0.1 °C. A saturated calomel electrode (SCE) was used as a reference electrode, and a graphite rod was used as a counter electrode. Potentials were reported *vs.* reversible hydrogen electrode (RHE) by adding 1.011 V.

Inks of the catalytic powders were prepared according to the following recipe: 0.80 mL of DDI water, 0.2 mL isopropanol, 20 μL of Nafion (5 wt% in water/isopropanol, Alfa Aeser), and 1.0 mg of NSiC-*T* powder, were mixed and sonicated for 30 min. 10 μL of the ink was drop-casted onto a polished glassy carbon rotating-disk electrode (φ = 5 mm, A = 0.196 cm^2) and dried at 50 °C in air. Another 10 μL drop of ink was applied to the electrode and dried at 50 °C under air. Thus, the total catalyst loading was 20 μg of catalyst material, giving a surface loading of 102 μg cm^{-2}.

Experiments were conducted in 0.1 M KOH at 25.0 °C, saturated by O_2 (for ORR studies) or N_2 (for baseline measurements) by bubbling the gas for 30 min, and then keeping the cell under a gas blanket. Currents in N_2-purged solutions were subtracted from those in the O_2-purged solutions, to account for capacitive currents. Linear scan RRDE voltammograms, performed on a rotating disk at rotation speeds of 400–2000 rpm and scan rate at 10 mV s^{-1}. The number of electrons transferred per O_2 molecule (n) was calculated by the Koutecký–Levich method from linear sweep voltammograms as described elsewhere.[33] The yield of H_2O_2 (%) was calculated by eqn (S1) (ESI†), where I_{ring} is the ring current, and I_{disk} is the disk current. The collection efficiency was determined experimentally to be

N = 0.35, using 4 mM of the Ru(III)/Ru(II) hexamine couple in N_2-purged 0.1 M KCl.

Material characterization

Powder X-ray diffraction (XRD) was performed in a Rigaku SmartLab X-ray diffractometer with Cu-Kα radiation (λ = 1.5418 Å), scan rate of 1° min^{-1}. High-resolution scanning electron microscopy (HRSEM) was performed in secondary-electron mode on a Zeiss Ultra+ microscope, at a 4 kV acceleration voltage. Elemental analysis was carried out at Microlab Kolbe in Oberhausen, Germany.

X-ray photoelectron spectroscopy (XPS) was collected on a PHI VersaProbe III scanning microprobe supplied from Physical Instruments at UHV (10^{-10} Torr), step size 0.05 eV. Peaks were calibrated using the C 1s position (284.5 eV), and deconvoluted in CasaXPS. Raman spectroscopy was performed on a Horiba LabRam HR Evolution Raman microscope using ×10 lens, 532 nm laser excitation wavelength, and 1800 grating.

N_2 adsorption–desorption isotherms (at 77 K) were measured on a Quantachrome Autosorb iQ instrument, using vacuum-dried samples (200 °C for 10 h). The isotherms were analyzed using the Brunauer–Emmett–Teller (BET) model for specific surface area (SSA, at P/P_0 values of 0.01–0.15) and quenched solid state density functional theory (QSDFT) isotherm fitting for meso–micropore size distribution. In the latter, the model used was N_2/carbon at 77 K, with slit-shaped pores, in equilibrium.

Results and discussion

Carbons doped by Si and N

To synthesize the NSiC, we adopted an existing procedure,[24] detailed in the ESI.† In short, a commercial silicon carbide matrix precursor (StarPCS™ SMP-10) and acrylonitrile were polymerized together under anaerobic conditions (75 °C for 20 h) and then pyrolyzed (T = 600, 700, 800, 900 and 1000 °C) to give the carbons NSiC-T, where T denotes the pyrolysis temperature. Since the silicon atoms are pre-dispersed in the polymer, we expect minimal segregation to SiO_2 during following thermal treatments. X-ray diffraction (XRD) of the materials shows four broad peaks at 9°, 16° and 27.5°, suggesting a partially graphitic carbon and no SiO_2 peaks (Fig. S1, ESI†).[4]

The electrochemical ORR on the Si-, N-co-doped carbons was studied by cyclic voltammetry (CV) on a rotating ring disk electrode (RRDE) in a three-electrode cell configuration, in 0.1 M KOH at 25 °C. In the absence of oxygen, the voltammograms of all NSiC-T materials show only non-faradaic currents for capacitive double layer charging, and some pseudocapacitive currents attributed to the N and O groups,[34] in the form of very broad peaks. In O_2-saturated solutions, all NSiC materials show ORR activity (I_{disc}, Fig. 1b) with concomitant production of H_2O_2 peroxide intermediates. This agrees with the RRDE measurements, suggesting that the 2/4 e$^-$ selectivity on these NSiC materials is governed by their ability to reduce the peroxide intermediate.

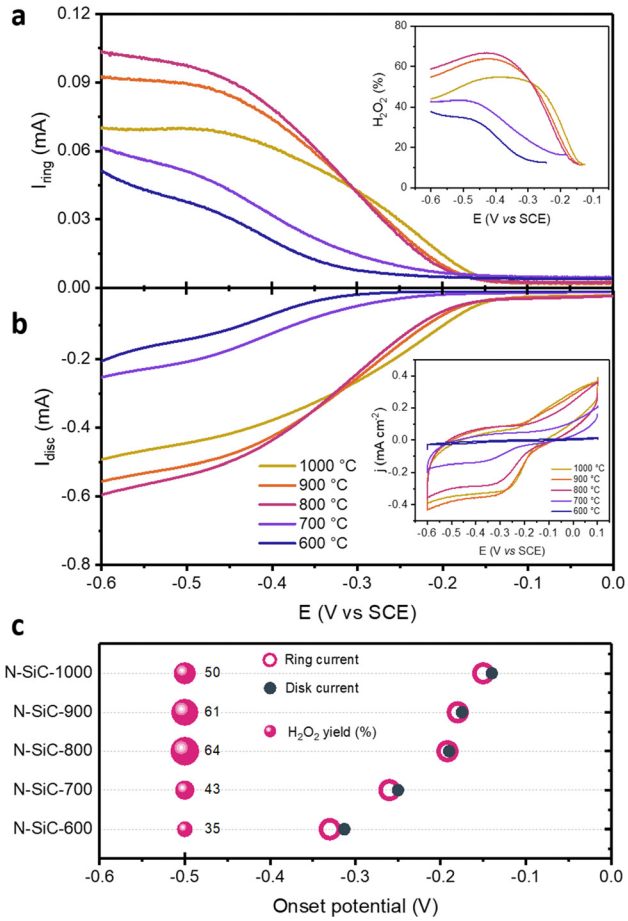

Fig. 1 (a) Linear scan RRDE voltammograms of NSiC-T, top: ring current, corrected by the collection factor of 0.35, (b): disk current. (a, inset) H_2O_2 yield *versus* potential. (b, inset) cyclic voltammogram of NSiC-T materials. (c) Onset potentials of I_{ring} and I_{disk}, and peroxide yield at constant potential (−0.5 V), for the different NSiC-T materials. T denotes pyrolysis temperature (°C). Measurements performed in O_2-saturated 0.1 M KOH at 25 °C, scan rate 10 mV s^{-1}, rotation speed 1600 rpm. Data is corrected for capacitive currents measured in a N_2-purged solution.

The onset for ORR on NSiC-600 and NSiC-700 shifts to more negative potentials compared to NSiC-800, -900, or -1000. Generally, the ORR on N-doped carbons proceeds *via* either a 4e$^-$ or 2e$^-$ pathway, generating H_2O (eqn (1) + (2), 4e$^-$ total) or H_2O_2 (eqn (1), 2e$^-$) as the final product (most typical to undoped carbons). However, nitrogen dopants (in particularly those in pyridinic positions in the lattice) can promote the disproportionation of peroxide (eqn (3)),[4] promoting effectively the 4e$^-$ pathway even in the absence of catalytic sites capable of performing the second 2e$^-$ reduction (eqn (2)).[35,36] Thus, the positive shift in onset potential on heating from 700 °C to 800 °C may be associated with the formation of beneficial nitrogen moieties. Since both disk and ring currents increase between NSiC-700 and NSiC-800, the H_2O_2 production also rises (Fig. 1a inset and Fig. 1c); however, heating the material to higher temperatures decreases the H_2O_2 yield again. The rising current densities also suggest a gradual change in the carbon structure, for example the clearing of pores from

pyrolysis products in the 700–800 °C range,[37] the partial collapse of micropores,[38] and the removal of some surface moieties (OH, =O, N–OH) contributing to wettability and adsorption. Higher temperatures also promote graphitization, which improves electronic conductivity (see Raman discussion below). Overall, there is a clear trend of more positive onset potential with pyrolysis temperature (Fig. 1c), with a maximum of peroxide yield in NSiC-800 (64% at –0.4 V *vs.* SCE). Before this maximum, insufficient peroxide is produced, while above this maximum, the peroxide is better activated (that is, decomposed and/or reduced).

To correlate the ORR activity to material morphology, we characterized the catalysts with high resolution scanning electron microscopy (HRSEM). This revealed all NSiC–*T* materials exhibit uniform porous structures with micro- and meso-porosity. The porosity is homogeneous across the pyrolysis temperature range (Fig. 2a–c). Raman spectroscopy shows typical carbon peaks, with D and G bands correlated to disordered and graphitic domains, respectively (Fig. S3, ESI†). Mathematical deconvolution of the bands showed that their intensity ratio (I_D/I_G) decreases with increasing pyrolysis temperature. This suggests that the aromaticity (sp^2) increases and the carbon defects are annealed with increasing pyrolysis temperature, leading to higher conductivity. Nitrogen adsorption isotherms were recorded at 77 K for all NSiC-*T* materials (Fig. 2d). The calculated Brunauer–Emmett–Teller (BET) specific surface areas (SSA) and pore distributions

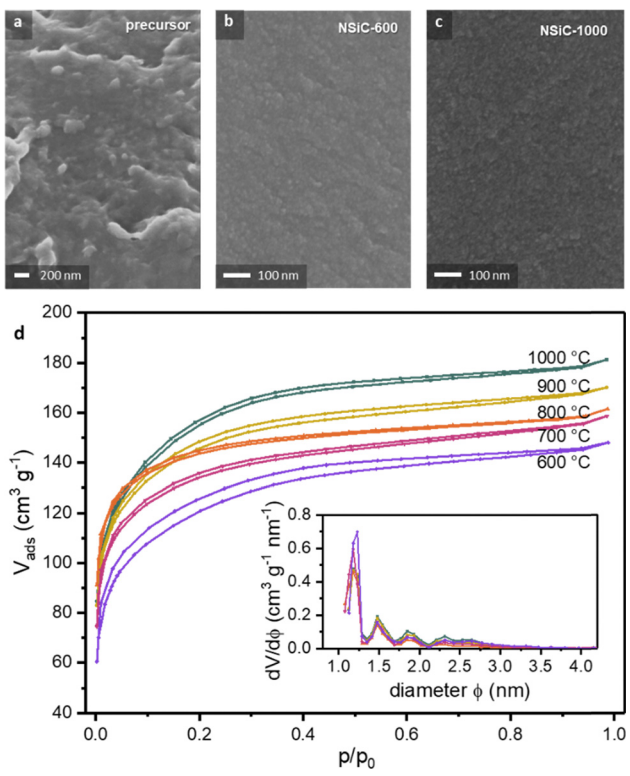

Fig. 2 Scanning electron micrographs of (a) the precursor material before pyrolysis and the carbon after pyrolysis at (b) 600 °C and (c) 1000 °C. (d) Adsorption–desorption isotherms on the NSiC-*T* carbons (N_2, 77 K). Inset: Pore size distributions calculated from the isotherms by NLDFT.

Table 1 Summary of the physical properties of NSiC-*T* materials

Carbon	Pyrolysis temperature [°C]	Surface area [m^2 g^{-1}]			Nitrogen content [wt%]
		Total	In micro-pores	In meso- pores	
NSiC-600	600	393	348	45	16.88
NSiC-700	700	422	388	34	14.61
NSiC-800	800	443	426	17	12.86
NSiC-900	900	463	425	38	10.75
NSiC-1000	1000	526	471	55	7.39

are summarized in Table 1. The nitrogen adsorption/desorption isotherms of NSiC-*T* are similar in shape. The type-I isotherm in the P/P_0 range 0.0–0.5 implies the existence of many micropores within the structure.[39] The NLDFT pore size distribution shows the majority of pores are micropores of the size 1.2–3.0 nm (Fig. 2d, inset).

Analysis of the pore distributions of the samples shows NSiC-*T* mainly contains micropores, with at most 4–11% mesopores by surface area (Table 1). Also, the total surface area of the NSiC-*T* materials increases with pyrolysis temperature, likely due to clearing of the micropores from amorphous "goo" formed during pyrolysis. It also confirms that the micropores are not collapsing yet, in contrast to other microporous carbons, where micropore collapse started already at 1000 °C.[38] This suggests that micropores are stabilized somehow by the Si-/N-co-doping. Since the surface area of NSiC-1000 is the largest, we decided to use this carbon for our metal dopant study.

Elemental analysis by inductively coupled plasma mass spectrometry (ICP-MS) revealed a high nitrogen content (7–17 wt%) which decreases with increasing pyrolysis temperature (Table 1). Even at 1000 °C there is still 7 wt% N, which is enough for good conductivity and electrocatalysis.[40] X-ray photoelectron spectroscopy (XPS) of the pristine NSiC-1000 material shows a surface coverage of N of about 3 at%. The N 1s region can be deconvoluted in five contributions: pyridinic N, pyridonic N, pyrolytic N, graphitic N and *N*-oxides (Fig. 3b).

The XPS spectra can also yield insights on possible interactions between the N and Si dopants. The Si 2p peak has five contributions (Fig. 3a): Si–C (100.8 eV), and Si–N (101.7 eV), Si^{3+}–O (103.2 eV), and Si^{4+}–O (103.5–104.8 eV).[41] The presence of SiN and SiC signals suggests that the Si is incorporated within the N-doped carbon structure, atomically and/or in carbide/nitride domains. The signal at 101.7 eV is attributed to the Si–N interaction, which is of relatively high intensity, suggesting the Si is in close contact with N. In the N 1s region, the N–Si peak is convoluted with pyridinic N (Fig. 3b), making cross-correlation difficult. Similarly, the Si–C signal in the C 1s region is overlapping with the 284.8 eV carbon signal.[42]

Carbons doped by Si, N, and Mn/Co/Ag

Co-doping the carbons with metals can improve their catalytic activity. We now consider three metals (Mn, Co and Ag), which are known to affect the ORR activity and $2e^-/4e^-$ selectivity, to co-dope the NSiC-*T* material. Manganese and nitrogen co-doping can yield Mn–N_4 sites that are highly active for the

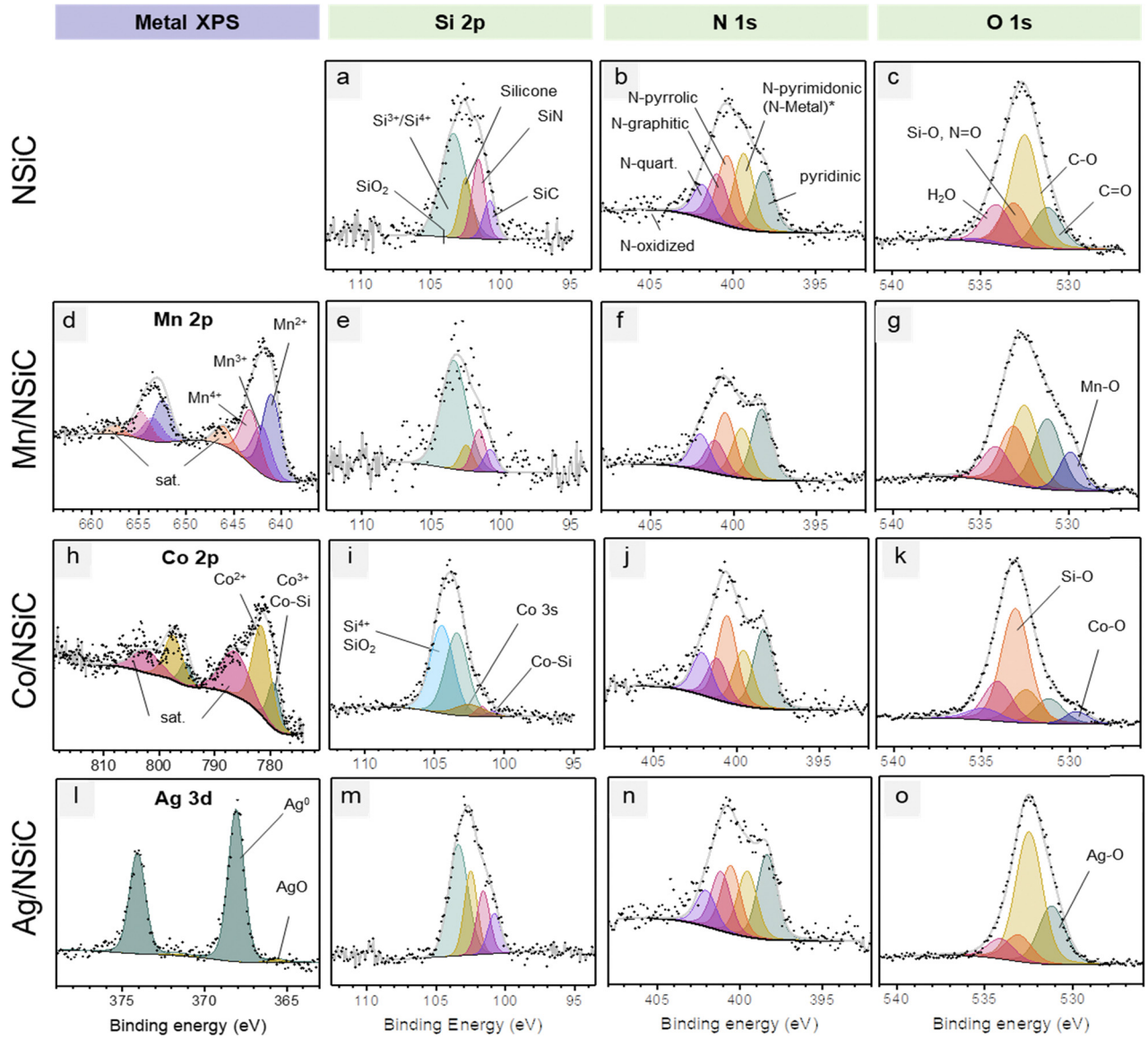

Fig. 3 X-ray photoelectron spectroscopy (XPS) of (a)–(c) NSiC-1000 in the (a) Si 2p, (b) N 1s and (c) O 1s regions; and of the (d)–(g) Mn-doped, (h)–(k) Co-doped, and (l)–(o) Ag-doped NSiC materials.

ORR.[43–46] Care must be taken, as these manganese sites often exhibit Fenton-like activity,[47,48] reacting with H_2O_2 in acid to produce OH radicals; although this will divert the ORR, such radicals may find use for oxidation reactions.[49] When combined with other metals, Mn can form bi-metallic clusters such as (N_3Co)–(MnN_3) within the carbon framework.[50,51] Cobalt is also known in ORR electrocatalysis, either as metallic Co or as cobalt oxides.[45] Co-doping of cobalt with N is very common, which can result in a variety of active phases (like Co_4N) or single-atom sites ($Co–N_4$) which catalyze the ORR.[52,53] The adjacent N-functionality determines the fate of the cobalt: pyrrole-type $Co–N_4$ groups increase H_2O_2 yield ($2e^-$ ORR) whereas pyridine-type $Co–N_4$ mainly catalyses the $4e^-$ ORR.[54]

Silver is an important element for ORR electrocatalysis,[55,56] being an affordable noble metal, hypothesized to boost the $4e^-$ ORR pathway.[57] In combining Si and Ag, one must beware that silicates are a known poison for Ag-catalysed ORR.[58] Thus, by first dispersing the Si throughout the NSiC carbon, we hope to limit metal silicate formation during any following thermal treatments. Silver doping of Mn_3O_4 shifts the d-band center of Mn and applies a strain which increases O–O bond split kinetics.[59] Moreover, Ag–Mn–O bonds that form in such silver–manganese oxides promote O_2 adsorption,[60,61] activation[62] and mobility.[63]

The metal doping was performed by incipient wetness impregnation of the metal nitrate solutions, followed by thermal treatment at 700 °C and reduction (H_2/N_2) at 550 °C. This method is known to form well-dispersed nanoparticles, which can interact with both the N and Si dopants.[64] ICP-MS measurements showed metal loadings of 4.0 wt% on all M/NSiC materials. The metal-loaded materials were analyzed by HRSEM, revealing nanoparticles in all three samples. Elemental mapping

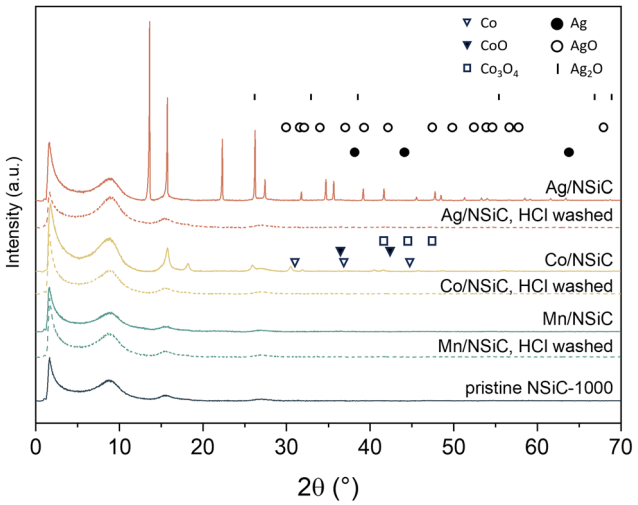

Fig. 4 X-ray diffractogram of metal-loaded Mn/NSiC-1000, Co/NSiC-1000, and Ag/NSiC-1000 before and after HCl washing. Peaks for the Ag phases were assigned using JCPDS cards #04-0783 (Ag), #01-074-1743 (AgO) and #041-1104 (Ag_2O). Peaks for the Co phases were assigned using JCPDS cards #05-727 (Co), #078-0431 (CoO) and #042-1467 (Co_3O_4).

by HRSEM-EDS confirmed that the metal is well-dispersed in the material (Fig. S4, ESI†). In the nanometer range however, some patches of surface were discovered which lacked nanoparticle coverage. The average recorded particle sizes were 15 nm ± 0.1 nm, 12.1 ± 0.1 nm and 50 nm ± 0.1 nm for Mn, Co and Ag, respectively. X-ray diffraction (XRD) of the Co and Ag materials showed sharp peaks indicating crystalline phases, attributed to the nanoparticles on the surface (Fig. 4). No crystalline manganese phases were detected. For comparison, the unimpregnated NSiC-*T* materials show only four broad signals, at 9°, 16° and 27.5°, independent of the pyrolysis temperature. The assignment of the peaks in XRD is difficult for the Co/NSiC sample, in part due to their low intensity. Possibly at the high pyrolysis temperatures, some complex mixed phases were developed, ranging from oxides to nitrides. Compared to the other sample, we see similar low angle peaks (15.7°, 18.2°) suggesting an ordering of about 0.5–0.56 nm. Powder XRD of the Ag/NSiC samples showed many sharp signals, attributed to metallic Ag, AgO and/or Ag_2O. The Co/NSiC signals are broader compared to Ag/NSiC, suggesting smaller particle size, or low crystallinity in the sample. We were unable to assign some peaks below 30°, probably arising from complex oxides in the multi-doped materials.

Electrochemical investigations into the ORR activity of the Mn-, Co- and Ag-impregnated samples, showed that I_{disk} rises when the metals (Mn, Co or Ag) were added to the NSiC support. This confirms that each of these 3 metals is beneficial for ORR electrocatalysis, each for its own reason. The Co/NSiC-1000 catalyst has an earlier (most positive) onset potential than either Ag/NSiC-1000 or Mn/NSiC-1000 (Fig. 5a). The fact that the onset of the ring currents on all M/NSiC-1000 materials is 40–80 mV more negative than the onset of the disk current indicates initial selectivity towards the $4e^-$ mechanism, making H_2O_2 only a side product at potentials <0.2 V. This is further confirmed by the H_2O_2 yield plot (Fig. 5c), showing that net H_2O_2 yield of all three impregnated samples is lower than the metal-free carbon throughout the potential range. Once potentials reach below –0.5 V, the Mn/NSiC-1000 catalyst has peroxide yields above those of NSiC-1000. Ag/NSiC-1000 has the same onset potential for the peroxide production as the Mn/NSiC-1000 but overall produces less H_2O_2 yield than both the starting material NSiC-1000 and Mn/NSiC-1000. Overall, all metals lower the peroxide yields in this potential range, while the Mn dopant increases it at large overpotentials. Specifically, the combination of MnO and Mn–N_x structures was reported to effectively suppress the H_2O_2 reduction reaction, leading to increased peroxide yields.[65] The mechanism behind this phenomenon at higher overpotentials is hypothesized to be linked to the amorphous nature of the Mn-doped structure, which provides a diverse array of active sites, becoming progressively accessible as the overpotential increases.

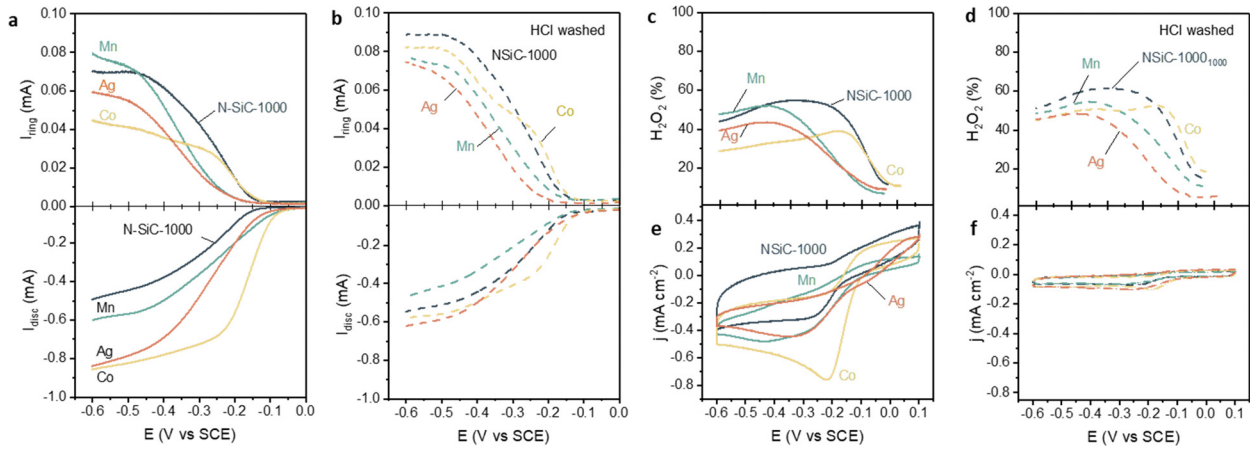

Fig. 5 Linear scan RRDE voltammograms of Mn/, Co/, and Ag/NSiC-1000, top: ring current, corrected by the collection factor of 0.35, bottom: disk current; (a) before and (b) after HCl wash. H_2O_2 yield *versus* potential for Mn/, Co/, and Ag/NSiCSC-1000 (c) before and (d) after HCl wash. Cyclic voltammogram of Mn/, Co/, and Ag/NSiC-1000 materials (e) before and (f) after HCl wash. Measurements performed in O_2-saturated 0.1 M KOH at 25 °C, scan rate 10 mV s^{-1}, rotation speed 1600 rpm. Data is corrected for capacitive currents measured in a N_2-purged solution.

The XPS analysis of the M/NSiC catalysts is shown in Fig. 3. One area of interest is the N 1s region (398.5–400 eV) where M–N interactions are located (Fig. 3b, f, j and n). For Mn, we don't expect a change in the N 1s spectrum.[7] However, the increase in signal for Co and Ag samples within this region may be because of convoluted M–N interactions (Fig. 3j and n). The Mn 2p region of the Mn/NSiC sample shows contribution from Mn^{2+} (640.8 eV), Mn^{3+} (642.3 eV) and Mn^{4+} (643.7 eV), but no Mn(0) (Fig. 3d). Although a quantitative assignment of Mn^{3+} is somewhat challenging, both Mn^{2+} and Mn^{4+} can be clearly assigned. After Mn-doping a new peak appears at 529.8 eV in the O 1s spectrum, corresponding to O–Mn bonds (Fig. 3g). This suggests that the Mn is present as a mixed oxide. In the Si 2p region, contributions from Si–C and Si–N arise from the support, while an increase in the Si–O components suggests further oxidation of the Si (Fig. 3e). This is further confirmed by the O 1s spectrum which shows a O–Si contribution (Fig. 3g). From Co 2p XPS we learn that the Co/NSiC sample consists of a mix of Co^{2+} and Co^{3+} likely as an oxide or oxyhydroxide species.[66] This is confirmed by the O 1s peak at 529.7 eV, characteristic of M–O interactions.[67] The Si 2p spectrum of Co/NSiC is convoluted by a broad underlying peak of Co 3s (Fig. 3i). The area was calculated based on the survey spectrum Co signals, with the position and full width half maximum (FWHM) fitted within literature values.[68] In Si 2p XPS we observe an increased contribution at 104.1 eV likely due to the formation of SiO_2,[69] which is matched with an increase of the Si–O contribution at 533.0 eV in the O 1s spectrum (*cf.* Fig. 3i and k). The Ag 3d XPS of Ag/NSiC sample shows a Ag^0 peak at 368.1 eV with a Ag $3d_{5/2}$–$3d_{3/2}$ splitting of 6.00 eV.[70] The $AgNO_3$ signal lies at a similar position, but due to the harsh temperature treatment during synthesis, we assume any $AgNO_3$ has fully converted into Ag^0, also no nitrate signal (>405 eV) was observed in the N 1s spectrum (Fig. 3l). The O 1s spectrum shows an increase of the O═C contribution, which can be attributed to O–Ag (Fig. 3o).[71] There is little change in the N 1s spectrum before and after Ag impregnation, so a M–N interaction cannot be excluded, although it is less likely.

To investigate how much of the observed activity is attributed to the metal dopant, we washed all catalysts with 1 M HCl and repeated the RRDE experiments. The HCl wash successfully removed all metallic and metal-oxide nanoparticles from the surface, as confirmed by XRD for both Ag/NSiC-1000 and Co/NSiC-1000 (Fig. 5b, d and f). Furthermore, HCl washing is non-oxidative and thus does not remove M–N sites,[72] enhancing the relative importance of M–N_x sites in catalysis. For Mn/NSiC-1000, the XRD analysis showed no change before and after washing, as it was amorphous to begin with; in any case, any Mn_xO_y that might have been on the surface, must have been removed.[73,74] Elemental analysis by ICP-MS confirms that the metal content drops from 4 wt% before the wash, to 0.10 wt% Mn, 0.58 wt% Ag, and 0.09 wt% Co after the wash. The remaining Ag must be amorphous phases encapsulated within the carbon, or bound to nitrogen moieties.[75–77]

Cyclic voltammetry of the HCl-washed materials revealed a steep decline in cathodic currents for all metal-impregnated samples (*cf.* Fig. 5e and f), confirming the role of the metallic nanoparticles in the ORR activity. Similarly, the RRDE measurements show lower I_{disk} on all HCl-washed materials (Fig. 5b). Interestingly, the onset potential for the lower currents remains the same before and after the HCl wash, suggesting that some metal remained on the surface (Fig. 6). The H_2O_2 yields increased after the metals were mostly removed by the HCl washing, approaching the values of the washed metal-free NSiC-1000 material. Interestingly, the HCl washing enhances the ORR activity of the NSiC-1000 catalyst, leading to higher H_2O_2 yields (Fig. 5b, d and Fig. 6). The acid washing could have removed oxygen and silicate moieties from the surface, clearing the surface area and enhancing mass transport through the porous network.

If one is interested in higher $2e^-$ selectivity (better H_2O_2 yields), a possible strategy could be based on Mn doping. Thus, we sought to study the effect of pyrolysis temperature on the activity of Mn/NSiC materials towards O_2 and H_2O_2 activation. We pyrolyzed the materials at 5 different temperatures, from 600 °C to 1000 °C, resulting in Mn/NSiC-*T* samples. The ORR disk currents on these materials were similar for the 700–1000 °C temperature range, while the onset potentials become gradually more positive with rising pyrolysis temperature (Fig. 7a). This suggests the catalytic activity is independent of the N content, which decreases with temperature; this, in turn, confirms that Mn–N coordination is not necessary for the ORR activity in these materials. However, this result may also be explained by an increasingly uneven distribution of particles.

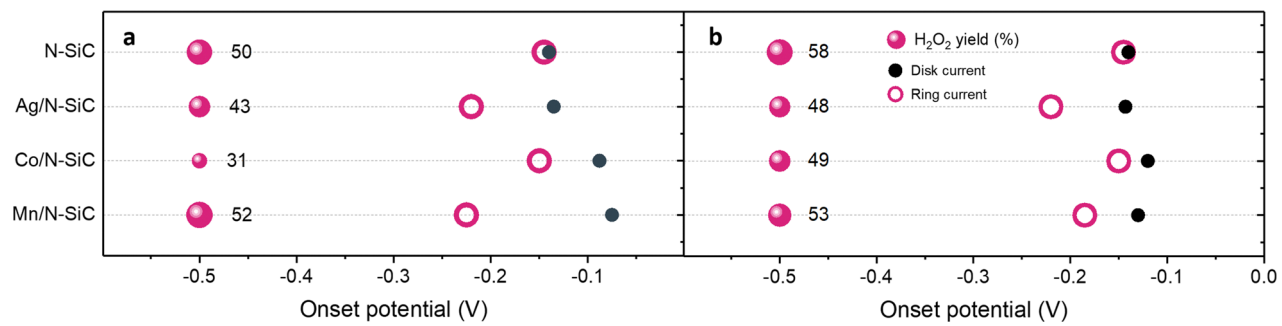

Fig. 6 Onset potentials of I_{ring} and I_{disk}, and peroxide yield at constant potential (−0.5 V), for the Ag/, Co/, and Mn/NSiC-1000 materials (a) before HCl wash and (b) after HCl wash.

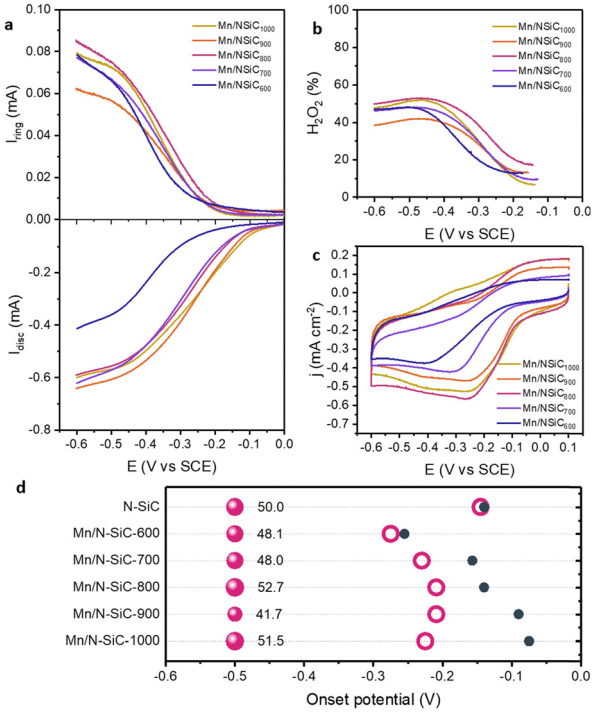

Fig. 7 (a) Linear scan RRDE voltammograms of Mn/NSiC-*T* materials, top: ring current, corrected by the collection factor of 0.35, bottom: disk current; and (b) H_2O_2 yield *versus* potential for Mn/NSiC-*T*. (c) Cyclic voltammogram of Mn/NSiC-*T* (no rotation). (d) Onset potentials of I_{ring} and I_{disk}, and peroxide yield at constant potential (−0.5 V), for the different Mn/NSiC-*T* materials. Measurements performed in O_2-saturated 0.1 M KOH at 25 °C, scan rate 10 mV s^{-1}, rotation speed 1600 rpm. Data is corrected for capacitive currents measured in a N_2-purged solution.

The ever-increasing gap between the onsets for O_2 activation and H_2O_2 production, plotted in Fig. 7d, suggests that the two phenomena are largely decoupled on these materials: increasing the pyrolysis temperature improves the first, without significant changes to the second.

Next, we wanted to understand the interactions between multiple metal co-dopants (Mn, Co, and Ag), in the presence of the Si- and N-co-dopants. We chose the pyrolysis temperature of 1000 °C, where the difference between the potentials for O_2 activation and H_2O_2 production is the largest (Fig. 7d). The three metals were combined in different ratios, starting with Mn/Co and Mn/Ag in a 1 : 1 ratio. Then, focusing on the most promising pair (Mn/Ag), we varied the Ag : Mn in ratios of 1 : 3, 1 : 1 and 3 : 1.

Elemental analysis (by ICP-MS) confirms the 1 : 1 metal ratio in Mn–Co/NSiC-1000 and in Mn–Ag/NSiC-1000 (Table S4, ESI†). Electron microscopy (HAADF-STEM) shows that in both Mn–Co/NSiC-1000 (Fig. S8, ESI†) and Mn–Ag/NSiC-1000 (Fig. S9, ESI†), the C, Mn, Ag, and Co elements are uniformly distributed throughout the material. In both, silicon and oxygen are mostly found on particle edges. This could result from topographical effects or from the formation of silica and metal oxide at the edges of the particles, as observed above on Mn/NSiC-1000. Powder XRD of the two catalysts showed an abundance of crystalline fractions for the Mn–Ag catalysts, which can be

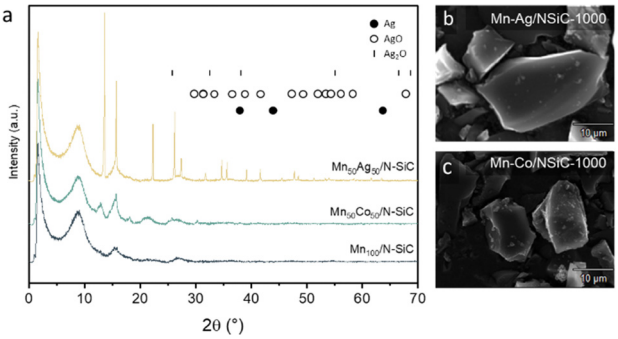

Fig. 8 (a) X-ray diffractogram of 1 : 1 combinations of Mn and Ag (Mn–Ag/NSiC-1000) and Mn and Co (Mn–Co/NSiC-1000). (b, c) STEM-HAADF image of the two materials.

attributed mainly to metallic Ag, AgO and Ag_2O (Fig. 8a).[78] The XRD diffractogram of Mn–Ag/NSiC-1000 is identical to that of Ag/NSiC, suggesting that no new crystalline alloys or mixed oxides form when Mn is added to the material. The Mn–Co/NSiC-1000 sample shows similar behaviour: after the thermal reduction, the XRD is identical to that of Co/NSiC-1000, with minimal crystallinity that is hard to assign (Fig. 8a).

XPS of the Mn/NSiC-1000, Mn–Co/NSiC-1000 and Co/NSiC-1000 shows specific contributions at 529.2 eV in the O 1s XPS, likely corresponding to an metal–O interaction (Fig. S7d, i and m, ESI†). Also, the Co may have an interaction with the SiO_2 signal at 105.1 eV (Fig. S7b, g and k, ESI†). The N 1s spectra of Mn/NSiC-1000, Mn–Co/NSiC-1000 and Co/NSiC-1000 do not show any changes compared with the unimpregnated NSiC-1000 sample. The Co 2p signal of Co–Mn/NSiC-1000 sample shifted by about 0.4 eV compared to the Co/NSiC-1000 sample, possibly resulting from a Mn–Co interaction.

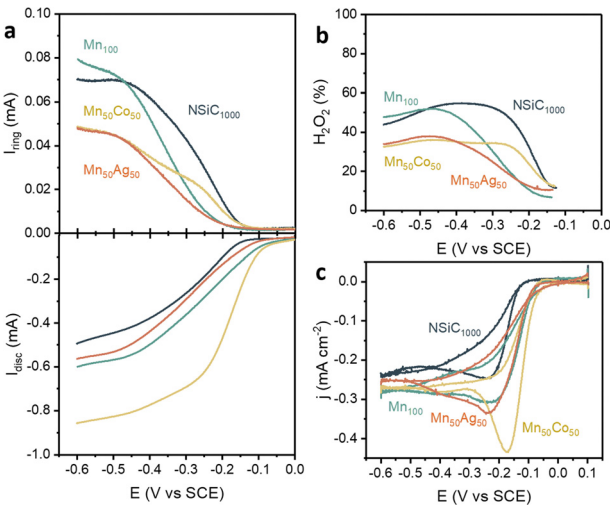

Fig. 9 (a) Linear scan RRDE voltammograms of Mn–Co/NSiC-1000 and Mn–Ag/NSiC-1000, top: Ring current, corrected by the collection factor of 0.35, bottom: Disk current. (b) H_2O_2 yield on Mn–Co/NSiC-1000 and Mn–Ag/NSiC-1000. Measurements performed in O_2-saturated 0.1 M KOH at 25 °C, scan rate 10 mV s^{-1}, rotation speed 1600 rpm. Data is corrected for capacitive currents measured in a N_2-purged solution. (c) Cyclic voltammograms of Mn–Co/NSiC-1000 and Mn–Ag/NSiC-1000 (no rotation).

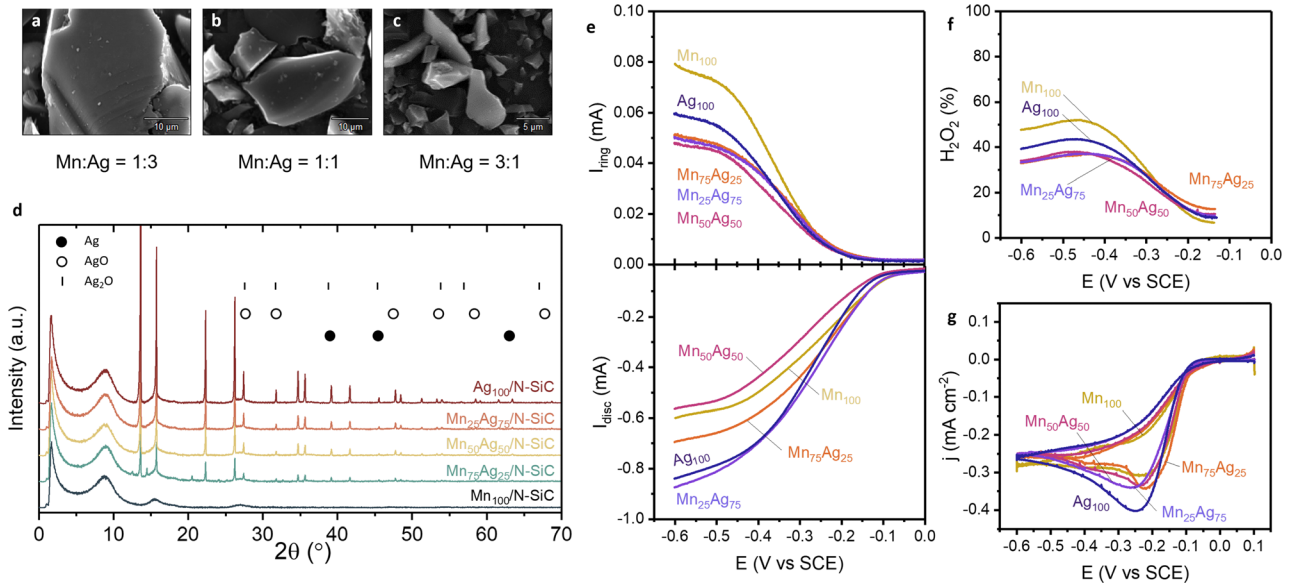

Fig. 10 HAADF-STEM images of (a) $Mn_{25}Ag_{75}$/NSiC-1000, (b) $Mn_{50}Ag_{50}$/NSiC-1000, and (c) $Mn_{75}Ag_{25}$/NSiC-1000 bimetallic catalysts. (d) X-ray diffractogram of Mn : Ag-loaded NSiC with different Mn : Ag ratios. (e) Linear scan RRDE voltammograms of Mn–Ag/NSiC-1000 bimetallic catalyst with different ratios of Mn and Ag (total metal loading 4 wt%), top: Ring current, corrected by the collection factor of 0.35, bottom: Disk current. (f) H_2O_2 yield on Mn–Ag/NSiC-1000 at different ratios. (g) Cyclic voltammograms of Mn–Ag/NSiC-1000 at different ratios (no rotation).

Electrochemical testing showed that the O_2 is activated at the same early potential (E_{onset} = −0.1 V *vs.* SCE) on both Mn–Co/NSiC-1000 and Mn–Ag/NSiC-1000 catalysts (Fig. 9a). Compared to the pure Mn, pure Ag, or pure Co catalysts, the mixed Mn–Ag or Mn–Co catalysts yield lower ORR currents (I_{disk}), but also lower H_2O_2 (Fig. 9b and c). Between them, $Mn_{50}Co_{50}$/NSiC-1000 produces more H_2O_2 than $Mn_{50}Ag_{50}$/NSiC-1000, but without a delay in the onset for peroxide production. This suggests that the ORR selectivity towards the $2e^-$ pathway is poor. $Mn_{50}Ag_{50}$/NSiC-1000 does show a delay in the peroxide production potential, and an overall lower peroxide yield, which makes this our prime candidate for further studies.

To further test the active combination Mn and Ag in the Si-, N-co-doped catalyst, we varied their ratio from 0% to 100% in steps of 25%. The ratios of Ag : Mn were confirmed by ICP-MS (Table S5, ESI†). X-Ray diffraction of the Mn–Ag catalysts show AgO_x signals, with the intensity proportional to the Ag content (Fig. 10d). HAADF-STEM analysis of the Mn–Ag mixed catalysts show that manganese and silver are distributed throughout in all Mn–Ag catalysts (Fig. S11, ESI†). Additional elemental mapping of the $Mn_{25}Ag_{75}$/NSiC-1000 shows carbon, nitrogen and silver are homogeneously distributed in the whole material (Fig. S10, ESI†). Mn is also well-dispersed, but some larger particles of around 50–75 nm were observed. Oxygen is similarly homogeneously distributed, but a higher concentration was observed in the region of the larger Mn particles, presumably Mn-oxides.

XPS analysis of the Mn–Ag/NSiC-1000 samples (Fig. 11) tells us that the Ag within the Ag–Mn mixed catalysts is mostly present as Ag^0 (368.2 eV), with possibly some AgO_x (367.6 eV) in samples Ag_{100}/NSiC-1000 and $Mn_{75}Ag_{25}$/NSiC-1000, as both contributions are difficult to deconvolute. In the samples $Mn_{25}Ag_{75}$/NSiC-1000 and $Mn_{50}Ag_{50}$/NSiC-1000, a clear shoulder peak at 369.6 eV is visible which hypothetically may be attributed to Ag–Si or Ag–Mn interactions. Both the Mn 2p and the N 1s spectrum show no significant changes over the concentration range. The O 1s spectra vary somewhat, but the changes are difficult to interpret. The O 1s spectrum does reveal a signal at 529.5 eV for the samples $Mn_{25}Ag_{75}$/NSiC-1000, $Mn_{75}Ag_{25}$/NSiC-1000 and Mn/NSiC-1000 which likely is because of some Mn oxide present in the sample. The Si 2p spectrum of $Mn_{75}Ag_{25}$/NSiC-1000 shows an additional signal at 98.4 eV, which could not be assigned (Fig. 11, Si 2p).

The Mn-rich catalysts ($Mn_{50}Ag_{50}$/NSiC-1000 and Mn_{100}/NSiC-1000) have the lowest disc currents for O_2 reduction, while the Ag-rich materials ($Mn_{25}Ag_{75}$/NSiC-1000 and Ag_{100}/NSiC-1000) have higher I_{disk} values (Fig. 10a). The peroxide yield remains constant throughout the 25–75% variation in Ag content, and lower than in either pure Mn or pure Ag doping (Fig. 10b). This suggests that Mn are similar to each other in their H_2O_2 production activity, yet their joint presence creates active sites that are more active towards the $4e^-$ reduction and/or H_2O_2 decomposition. Without rotation, $Mn_{50}Ag_{50}$/NSiC-1000 shows the highest reduction peak, but only marginally larger than the others (Fig. 10c).

Conclusions

We have synthesized carbon materials co-doped with silicon and nitrogen (NSiC) at different pyrolysis temperatures (600–1000 °C), and used them as supports for a range of catalytic metals (Ag, Co, Mn) in different combinations. We studied their electrochemical activity towards the oxygen reduction reaction in alkaline environment, as a means of determining their ability to activate O_2 and subsequently to produce and further reduce H_2O_2. The carbons reached surface areas of 400–530 $m^2\ g^{-1}$

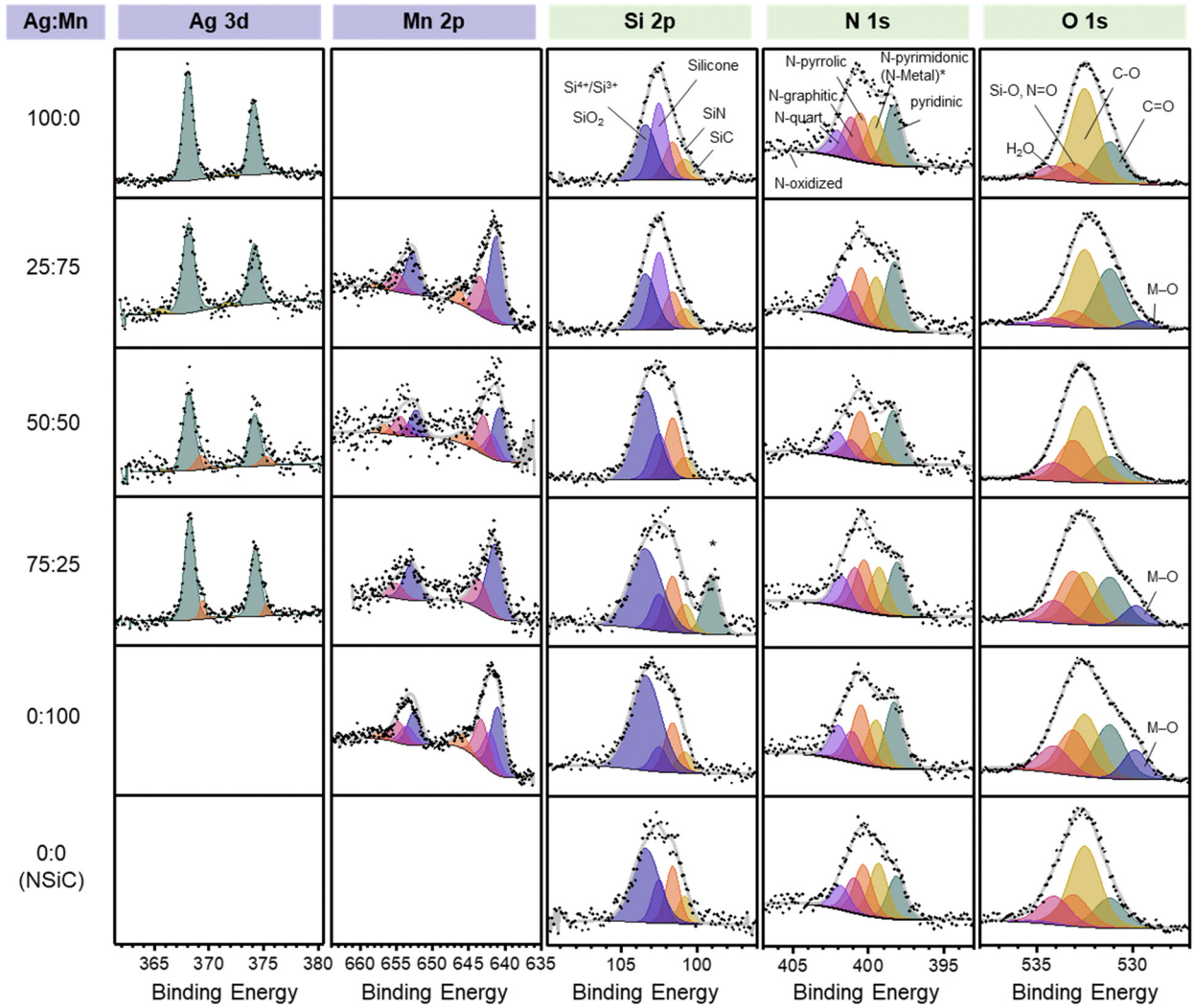

Fig. 11 XPS spectra of Mn : Ag/NSiC in five different ratio's (100 : 0, 75 : 25, 50 : 50, 25 : 75, 0 : 100) and pristine NSiC-1000 (bottom row).

(increasing with pyrolysis temperature) and high nitrogen content (17–7 wt%, decreasing with temperature). The ORR activity is significantly better (earlier onsets and higher currents) above 800 °C, with mostly $2e^-$ reduction to peroxide. When doping with Mn, Ag and Co, the onset for peroxide production was delayed, indicating a switch to $4e^-$ reduction and/or peroxide decomposition; with Co, the peroxide yields were the lowest (31% at –0.5 V *vs.* SCE). The highest peroxide production was on the Mn-doped material, probably due to MnO_x particles rather than Mn–N_x centers. In the multi-doped materials, $Ag_{25}Mn_{75}$/NSiC-1000 was found to have the highest ORR rates and lowest peroxide yields. Overall, we hope that these results will allow for better use of such multi-doped supports for reductive catalysis.

Author contributions

T. S. synthesized the materials, performed the electrochemical measurements (with the help of Y. S.) and the material characterizations (with the help of K. I.). T. K. S. analyzed the results and wrote the article. R. K. provided resources. D. E. supervised the project and edited the article text. All authors contributed to editing the article.

Data availability

All the data supporting this article are within the article itself.

Conflicts of interest

There are no conflicts to declare.

Acknowledgements

We thank the Israel Ministry of Energy (grant 218-11-024) for partial funding. T. S. thanks the Elite Network of Bavaria and Minerva Short-Term Research Grant for financial support. T. K. S. thanks the Azrieli Foundation and the Israel Academy of Science and Humanities for post-doctoral fellowships. R. K

thanks the German Research Foundation CRC 1585 A 02 (492723217) for financial support.

References

1 S. Schwarz, M. Friedrich, G. Motz and R. Kempe, *Z. Anorg. Allg. Chem.*, 2015, **641**, 2266–2271.
2 M. Elfinger, T. Schönauer, S. L. J. Thomä, R. Stäglich, M. Drechsler, M. Zobel, J. Senker and R. Kempe, *ChemSusChem*, 2021, **14**, 2360–2366.
3 T. Irrgang and R. Kempe, *Chem. Rev.*, 2019, **119**, 2524–2549.
4 D. Eisenberg, W. Stroek, N. J. Geels, C. S. Sandu, A. Heller, N. Yan and G. Rothenberg, *Chem. – Eur. J.*, 2016, **22**, 501–505.
5 T. K. Slot, D. Eisenberg, D. van Noordenne, P. Jungbacker and G. Rothenberg, *Chem. – Eur. J.*, 2016, **22**, 12307–12311.
6 T. K. Slot, F. Yue, H. Xu, E. V. Ramos-Fernandez, A. Sepúlveda-Escribano, Z. Sofer, G. Rothenberg and N. R. Shiju, *2D Mater.*, 2020, **8**, 015001.
7 D. Eisenberg, T. K. Slot and G. Rothenberg, *ACS Catal.*, 2018, **8**, 8618–8629.
8 T. K. Slot, D. Eisenberg and G. Rothenberg, *ChemCatChem*, 2018, **10**, 2119–2124.
9 S. Zaman, L. Huang, A. I. Douka, H. Yang, B. You and B. Y. Xia, *Angew. Chem.*, 2021, **133**, 17976–17996.
10 B. Ge, L. Hu, X. Yu, L. Wang, C. Fernandez, N. Yang, Q. Liang and Q.-H. Yang, *Adv. Mater.*, 2024, **36**, 2400937.
11 E. V. Timofeeva, C. U. Segre, G. S. Pour, M. Vazquez and B. L. Patawah, *Curr. Opin. Electrochem.*, 2023, **38**, 101246.
12 M. Mazzucato, A. Facchin, M. Parnigotto and C. Durante, *ACS Catal.*, 2024, **14**, 6369–6403.
13 F. Rodŕíguez-Reinoso and A. Sepulveda-Escribano, in *Carbon Materials for Catalysis*, John Wiley & Sons, Ltd, 2008, pp. 131–155.
14 C. E. Banks, T. J. Davies, G. G. Wildgoose and R. G. Compton, *Chem. Commun.*, 2005, 829–841.
15 X. Xie, H. Peng, G. Ma, Z. Lei and Y. Xu, *Mater. Chem. Front.*, 2023, **7**, 2595–2619.
16 X. Feng, Y. Bai, M. Liu, Y. Li, H. Yang, X. Wang and C. Wu, *Energy Environ. Sci.*, 2021, **14**, 2036–2089.
17 X. Li, G. Liu, H. Zheng, K. Sun, L. Wan, J. Cao, S. Asif, Y. Cao, W. Si, F. Wang and A. Bokhari, *Energies*, 2023, **16**, 128.
18 Y. Wang, D. Wang and Y. Li, *Adv. Mater.*, 2021, **33**, 2008151.
19 Y. Zhou, R. Lu, X. Tao, Z. Qiu, G. Chen, J. Yang, Y. Zhao, X. Feng and K. Müllen, *J. Am. Chem. Soc.*, 2023, **145**, 3647–3655.
20 Y. Zeng, C. Li, B. Li, J. Liang, M. J. Zachman, D. A. Cullen, R. P. Hermann, E. E. Alp, B. Lavina, S. Karakalos, M. Lucero, B. Zhang, M. Wang, Z. Feng, G. Wang, J. Xie, D. J. Myers, J.-P. Dodelet and G. Wu, *Nat. Catal.*, 2023, **6**, 1215–1227.
21 P. Ye, K. Fang, H. Wang, Y. Wang, H. Huang, C. Mo, J. Ning and Y. Hu, *Nat. Commun.*, 2024, **15**, 1012.
22 S. K. Kaiser, Z. Chen, D. Faust Akl, S. Mitchell and J. Pérez-Ramírez, *Chem. Rev.*, 2020, **120**, 11703–11809.
23 S. H. Al-Hilfi, X. Jiang, J. Heuer, S. Akula, K. Tammeveski, G. Hu, J. Yang, H. I. Wang, M. Bonn, K. Landfester, K. Müllen and Y. Zhou, *J. Am. Chem. Soc.*, 2024, **146**, 19886–19895.
24 T. Schönauer, S. L. J. Thomä, L. Kaiser, M. Zobel and R. Kempe, *Chem. – Eur. J.*, 2021, **27**, 1609–1614.
25 C. Chowdhury and A. Datta, *J. Phys. Chem. C*, 2018, **122**, 27233–27240.
26 A. Eljarrat, L. López-Conesa, J. López-Vidrier, S. Hernández, B. Garrido, C. Magén, F. Peiró and S. Estradé, *Nanoscale*, 2014, **6**, 14971–14983.
27 V. Khaki, M. T. Ahmadi, M. Hassanzadazar and T. K. Nguyen, *J. Electron. Mater.*, 2021, **50**, 2903–2910.
28 P. Zhang, X. Hou, J. Mi, Y. He, L. Lin, Q. Jiang and M. Dong, *Phys. Chem. Chem. Phys.*, 2014, **16**, 17479–17486.
29 X. Fu, Q.-D. Wang, Z. Liu and F. Peng, *Mater. Lett.*, 2015, **158**, 32–35.
30 K. Kaare, M. Jantson, R. Palgrave, M. Tsujimoto, A. Kuzmin, B. Shainyan and I. Kruusenberg, *J. Electroanal. Chem.*, 2023, 117859.
31 B. Sungur, Ç. Kızıl and E. Bayram, *Int. J. Hydrogen Energy*, 2023, **48**, 17512–17525.
32 E. I. Solomon and S. S. Stahl, *Chem. Rev.*, 2018, **118**, 2299–2301.
33 D. Eisenberg, W. Stroek, N. J. Geels, S. Tanase, M. Ferbinteanu, S. J. Teat, P. Mettraux, N. Yan and G. Rothenberg, *Phys. Chem. Chem. Phys.*, 2016, **18**, 20778–20783.
34 J. Biemolt, I. M. Denekamp, T. K. Slot, G. Rothenberg and D. Eisenberg, *ChemSusChem*, 2017, **10**, 4018–4024.
35 J. D. Wiggins-Camacho and K. J. Stevenson, *J. Phys. Chem. C*, 2011, **115**, 20002–20010.
36 S. Maldonado and K. J. Stevenson, *J. Phys. Chem. B*, 2005, **109**, 4707–4716.
37 Y. Chen, Z. Yin, F. Sun, H. Xu, J. Wu and F. Fu, *Energy Explor. Exploit.*, 2023, **41**, 154–169.
38 D. Eisenberg, P. Prinsen, N. J. Geels, W. Stroek, N. Yan, B. Hua, J.-L. Luo and G. Rothenberg, *RSC Adv.*, 2016, **6**, 80398–80407.
39 M. Thommes, K. Kaneko, A. V. Neimark, J. P. Olivier, F. Rodriguez-Reinoso, J. Rouquerol and K. S. W. Sing, *Pure Appl. Chem.*, 2015, **87**, 1051–1069.
40 E. V. Suslova, E. A. Arkhipova, A. V. Kalashnik, A. S. Ivanov, S. V. Savilov, H. Xia and V. V. Lunin, *Russ. J. Phys. Chem. A*, 2019, **93**, 1952–1956.
41 C. Qin, G. Wen, X. Wang, L. Song and X. Huang, *J. Mater. Chem.*, 2011, **21**, 5985–5991.
42 M. Y. Bashouti, Y. Paska, S. R. Puniredd, T. Stelzner, S. Christiansen and H. Haick, *Phys. Chem. Chem. Phys.*, 2009, **11**, 3845–3848.
43 E. Y. Choi, D. E. Kim, S. Y. Lee, C. B. Park and C. K. Kim, *Appl. Catal., B*, 2023, **325**, 122386.
44 S. Kim, S. Ji, H. Yang, H. Son, H. Choi, J. Kang and O. L. Li, *Appl. Catal., B*, 2022, **310**, 121361.
45 X. Zhou, X. Liu, J. Zhang, C. Zhang, S. J. Yoo, J.-G. Kim, X. Chu, C. Song, P. Wang, Z. Zhao, D. Li, W. Zhang and W. Zheng, *Carbon*, 2020, **166**, 284–290.
46 Z. Wang, P. Yan, D. Deng, L. Xu and H. Li, *Energy Fuels*, 2024, **38**, 10589–10612.
47 J. Shi, S. Deng, X. Hu, X. Sun, S. Zhou, L. Fan, W. Cai and J. Li, *Energy Fuels*, 2022, **36**, 8432–8438.

48 J. Li, M. Chen, D. A. Cullen, S. Hwang, M. Wang, B. Li, K. Liu, S. Karakalos, M. Lucero, H. Zhang, C. Lei, H. Xu, G. E. Sterbinsky, Z. Feng, D. Su, K. L. More, G. Wang, Z. Wang and G. Wu, *Nat. Catal.*, 2018, **1**, 935–945.
49 X. Han, T. Zhang, W. Chen, B. Dong, G. Meng, L. Zheng, C. Yang, X. Sun, Z. Zhuang, D. Wang, A. Han and J. Liu, *Adv. Energy Mater.*, 2021, **11**, 2002753.
50 G. Dey, R. Jana, S. Saifi, R. Kumar, D. Bhattacharyya, A. Datta, A. S. K. Sinha and A. Aijaz, *ACS Nano*, 2023, **17**, 19155–19167.
51 N. Reddy Samala and I. Grinberg, *ChemSusChem*, 2022, **15**, e202200795.
52 Y. Yang, R. Zeng, Y. Xiong, F. J. DiSalvo and H. D. Abruña, *J. Am. Chem. Soc.*, 2019, **141**, 19241–19245.
53 P. Rao, D. Wu, T.-J. Wang, J. Li, P. Deng, Q. Chen, Y. Shen, Y. Chen and X. Tian, *eScience*, 2022, **2**, 399–404.
54 S. Chen, T. Luo, X. Li, K. Chen, J. Fu, K. Liu, C. Cai, Q. Wang, H. Li, Y. Chen, C. Ma, L. Zhu, Y.-R. Lu, T.-S. Chan, M. Zhu, E. Cortés and M. Liu, *J. Am. Chem. Soc.*, 2022, **144**, 14505–14516.
55 N. A. Shumilova, G. V. Zhutaeva and M. P. Tarasevich, *Electrochim. Acta*, 1966, **11**, 967–974.
56 P. K. Adanuvor and R. E. White, *J. Electrochem. Soc.*, 1988, **135**, 2509.
57 A. Zhang, Y. Liu, C. Li, L. Xue, Z. Liu, J. Wu and S. Zeng, *Green Energy Environ.*, 2023, **8**, 1437–1449.
58 J. Guo, A. Hsu, D. Chu and R. Chen, *J. Phys. Chem. C*, 2010, **114**, 4324–4330.
59 S.-A. Park, H. Lim and Y.-T. Kim, *ACS Catal.*, 2015, **5**, 3995–4002.
60 I. Shypunov, N. Kongi, J. Kozlova, L. Matisen, P. Ritslaid, V. Sammelselg and K. Tammeveski, *Electrocatalysis*, 2015, **6**, 465–471.
61 H. Huang, Y. Meng, A. Labonte, A. Dobley and S. L. Suib, *J. Phys. Chem. C*, 2013, **117**, 25352–25359.
62 S. Hu, J. Zhang, X. Chen, X. Qin, J. Yao and C. Zhang, *J. Environ. Sci.*, 2024, **138**, 709–718.
63 B. Li, F. Deng, Z. Li, H. Xiong, S. Zhang, W. Dai, J. Zhang, L. Yang, J. Zou and X. Luo, *Sep. Purif. Technol.*, 2023, **320**, 124240.
64 M. Elfinger, T. Schönauer, S. L. J. Thomä, R. Stäglich, M. Drechsler, M. Zobel, J. Senker and R. Kempe, *ChemSusChem*, 2021, **14**, 2360–2366.
65 A. Byeon, J. Cho, J. Min Kim, K. Hwa Chae, H.-Y. Park, S. Won Hong, H. Chul Ham, S. Woo Lee, K. Ro Yoon and J. Young Kim, *Nanoscale Horiz.*, 2020, **5**, 832–838.
66 M. C. Biesinger, B. P. Payne, A. P. Grosvenor, L. W. M. Lau, A. R. Gerson and R. S. C. Smart, *Appl. Surf. Sci.*, 2011, **257**, 2717–2730.
67 A. N. Naveen and S. Selladurai, *Electrochim. Acta*, 2014, **125**, 404–414.
68 H. Seo, H.-R. Yang, Y. Yang, K. Kim, S. H. Kim, H. Lee and J.-H. Kim, *Materials*, 2021, **14**, 5397.
69 G. Zheng, Y. Xiang, L. Xu, H. Luo, B. Wang, Y. Liu, X. Han, W. Zhao, S. Chen, H. Chen, Q. Zhang, T. Zhu and Y. Yang, *Adv. Energy Mater.*, 2018, **8**, 1801718.
70 J. S. Hammond, S. W. Gaarenstroom and N. Winograd, *Anal. Chem.*, 1975, **47**, 2193–2199.
71 A. I. Boronin, S. V. Koscheev and G. M. Zhidomirov, *J. Electron Spectrosc. Relat. Phenom.*, 1998, **96**, 43–51.
72 T. Y. Burshtein, D. Aias, J. Wang, M. Sananis, E. M. Farber, O. M. Gazit, I. Grinberg and D. Eisenberg, *Phys. Chem. Chem. Phys.*, 2021, **23**, 26674–26679.
73 Md. A. Islam and M. M. Rahman, *Russ. J. Phys. Chem. A*, 2015, **89**, 706–709.
74 W. B. Holmes, *J. Am. Chem. Soc.*, 1907, **29**, 1277–1288.
75 X.-H. Jiang, L.-S. Zhang, H.-Y. Liu, D.-S. Wu, F.-Y. Wu, L. Tian, L.-L. Liu, J.-P. Zou, S.-L. Luo and B.-B. Chen, *Angew. Chem., Int. Ed.*, 2020, **59**, 23112–23116.
76 R. Zhou and S. Z. Qiao, *Chem. Mater.*, 2014, **26**, 5868–5873.
77 Y. Chen, R. Guo, X. Peng, X. Wang, X. Liu, J. Ren, J. He, L. Zhuo, J. Sun, Y. Liu, Y. Wu and J. Luo, *ACS Nano*, 2020, **14**, 6938–6946.
78 T. Liu, X. Li and F. Li, *Environ. Sci. Technol.*, 2008, **42**, 4540–4545.

